



Humidity-Activated Shape Memory Effects on Thermoplastic Starch/EVA Blends and Their Compatibilized Nanocomposites

Valentina Sessini, Jean-Marie Raquez,* Denis Lourdin, Jean-Eudes Maigret, José Maria Kenny, Philippe Dubois, and Laura Peponi*

In this work, a systematic study on the humidity-activated shape memory properties of dual-responsive shape memory bionanocomposites with both humidity- and thermally-activated shape memory effects is reported. The study is performed through humidity-mechanical cycles in an Instron machine with a temperature chamber equipped with an ultrasonic humidity generator. In particular, the bionanocomposites studied are based on blends of ethylene–vinyl acetate (EVA) and thermoplastic starch reinforced with natural bentonite. In our previous work, thermomechanical cycles are performed by using EVA-induced crystallization and a preliminary humidity-activated shape memory test is designed. Herein, the shape memory results of both blends and their nanocomposites reflect the very good ability to humidity-activated recover of the initial shape with values higher than 80%. Moreover, the ability to fix the temporary shape of this systems is very good, especially when nanofillers are added. The compatibilizer effect of natural bentonite is demonstrated by means of different techniques such as scanning emission microscopy and mapping by confocal Raman spectroscopy.

1. Introduction

The continuous demand for new engineering materials with high performance and different functionalities is leading to the development of new smart multifunctional materials, more particularly the so-called “shape memory” materials, including shape memory polymers (SMPs), metal alloys, hybrids, ceramics, and gels.^[1,2] SMPs are polymeric smart materials capable to memorize temporary shapes and recover their original shape upon external stimulation, including temperature, light, humidity, pH, electric or magnetic field, etc.^[3] In general, SMPs are strongly affected by the molecular structure of the polymer and they can be programmed in order to exhibit shape memory properties, i.e., combining the effect of two polymer domains/segments or phases.^[4] One is the “fixity domain,”

typically imparted by a network structure that involves covalent or physical crosslinks, and the “switching domain” able to fix the temporary shape. The switching domain is characterized by a reversible phase transition.^[5]

SMPs used for advanced medical application (smart stents, sutures, and other invasive devices) must satisfy some specific requirements such as no toxicity for the human body, sterilizability, eventual biodegradability/bioresorbability under physiological conditions, and biocompatibility, while depending on the application, the thermal activation is required to be near to the human body temperature without external heating.^[6] With the aim to overcome this limitation, other strategies have been developed, among which the moisture-activation of the SMPs.^[7] In fact, in order to develop humidity-activated SMPs it is possible to use polymers with functional groups able to be involved in hydrogen bonding with water molecules or it is possible to use hydrophilic component. Further investigations showed that the hydrogen bonding is the key player behind the water-activation and water or humidity absorbed in the polymer plays a main role in the shape recovery process.^[8] With this purpose, for the last years, the interest paid in the developments of new multifunctionally tailored materials, obtained by applying nanotechnologies as well as by using environmentally friendly


Dr. V. Sessini, Prof. J. M. Kenny
Dipartimento di Ingegneria Civile e Ambientale
Università di Perugia

Strada di Pentima 05100, Terni, Italy

Dr. V. Sessini, Dr. L. Peponi
Instituto de Ciencia y Tecnología de Polímeros
ICTP-CSIC
calle Juan de la Cierva 3, 28006 Madrid, Spain
E-mail: lpeponi@ictp.csic.es

Dr. J.-M. Raquez, Prof. P. Dubois
Laboratory of Polymeric and Composite Materials
University of Mons – UMONS
Place du Parc 23, B-7000 Mons, Belgium
E-mail: jean-marie.raquez@umons.ac.be

Prof. D. Lourdin, Dr. J.-E. Maigret
INRA
UR1268
Unité Biopolymères Interactions et Assemblages
44300, Nantes, France

 The ORCID identification number(s) for the author(s) of this article can be found under <https://doi.org/10.1002/macp.201700388>.

DOI: 10.1002/macp.201700388

approaches, such as renewal sources, biodegradable, biocompatible materials, etc. has strongly increased.^[9,10]

Among natural biopolymers, starch is attracting the interest of scientists as well as of industry due to its complete biodegradability, low cost, and renewability.^[11] Starch is mainly composed by two structurally distinct α -D-glucan components: amylose, which is linear, and amylopectin, which is highly branched.^[12] Although starches from different botanical origins present identical structural units, their amylose and amylopectin contents change, strongly influencing their physical and chemical properties. Moreover, it is well known that, depending on the botanic origin of starch (i.e., potato, maize, pea, rice, barley, etc.), native granules present a wide variety of size (2–100 μm), size distribution, shape, extraction from plant conversion factors, and chemical composition. Furthermore, both amylose content and botanic origin considerably influence its crystalline organization.^[13] Although starch can be used as filler,^[14] thermoplastic starch (TPS) is preferred to be used as polymeric matrix after melt-processing native starch with plasticizer such as glycerol and water.^[15] Its T_g is strongly affected by the relative humidity (RH) at which it is stored showing either a glass-like rigid and fragile mechanical behavior, or rubber-like behavior depending on its moisture conditions.^[16] Its high water sensitivity tends to make TPS poorly competitive for the replacement of oil-based thermoplastic applications. However, from the other hand, its moisture sensitivity can be an advantage for the design of humidity-responsive functional materials.^[17] Furthermore, in commercial application, TPS is blended with other synthetic and bio-based polymers in order to improve its poor mechanical properties and high moisture sensitivity.^[18]

Among biocompatible polymers, ethylene–vinyl acetate copolymer (EVA) is a low cost commodity polymer that has found a wide industrial usage.^[19] EVA is a copolymer of ethylene and vinyl acetate (VA) with a random incorporation of VA comonomer units into polyethylene (PE) backbones.^[20] The VA content typically varies from 10 to 40 wt% strongly affecting the final EVA properties. Thus, EVA with a low VA content (<20%) are usually used as thermoplastic and those with a higher VA content are used as oil-resistance elastomers.^[21–23] Since EVA is biocompatible, it has been used in many biomedical engineering applications, such as in drug delivery devices^[24] and shape memory applications.^[20,25]

In particular, in our previous communication^[1] we reported the ability of bionanocomposites based on blends of EVA and TPS reinforced with natural bentonite (CLNa⁺) to present dual-responsive shape memory effects. In fact, they were designed in order to present both thermally activated shape memory effects due to the EVA-induced crystallization as well as humidity-activated shape memory behavior due to the presence of TPS demonstrated in preliminary tests. In this work, we intend to study in a systematic way the humidity-activated behavior of EVA–TPS blends and their nanocomposites upon humidity-mechanical cycles as performed in an Instron machine with a temperature chamber equipped with an ultrasonic humidity generator. Moreover, the morphology, the thermal and mechanical properties of these materials were deeply studied, focusing the attention on the effects of the addition of nanoclays in the blend compatibility, and in

the humidity-activated shape memory properties of the final bionanocomposites.

2. Experimental Section

2.1. Materials

Native pea starch was obtained from Cosucra groupe Warcoing SA, Belgium, with a dry content of 85 wt%, including 60.7 wt% amylopectin, 35.7 wt% amylose, 3.4 wt% fiber, and 0.24 wt% protein, as determined by colorimetric methods and Proskey and DUMAS methods.^[26] Starch was used as received. Commercial EVA copolymer with 19 wt% VA content was purchased from Exxon Mobil Chemical Company. Glycerol (purity 97%) was purchased from VWR International and was used as starch plasticizer. Commercial natural bentonite, Cloisite-Na⁺ (CLNa⁺) was purchased from BYK Additives and Instruments. Its dimensions are typically ranging from 2 to 13 μm .

2.2. Starch-Based Blends and Nanocomposites Processing

Two different blends with different TPS content, i.e., 40 and 50 wt%, were processed and characterized, as well as their nanocomposites reinforced with 1 wt% of CLNa⁺. The processing method used was reported elsewhere.^[1] Briefly, first, the thermo-mechanical destructure of native starch granules with liquid glycerol and distilled water (in the wt ratio of 100:25:20) was performed in a Brabender internal kneader (for 3 min at 110 °C with a rotor speed of 100 rpm) in order to obtain thermoplastic starch. Once obtained TPS, it was melt blended with the commercial EVA with a twin-screw DSM microcompounder for 5 min at 160 °C with a screw speed of 125 rpm. Therefore, the blends with 40 and 50 wt% of TPS were obtained and named B40TPS and B50TPS, respectively. When the nanocomposites had been processed, CLNa⁺ nanoclays were used as nanofillers and were prior mixed with TPS through melt intercalation method in such a way to mix them with glycerol for a better clay dispersion. Two different nanocomposites, with 1 wt% of CLNa⁺ were obtained, named B50TPS + 1% CLNa⁺ and B40TPS + 1% CLNa⁺. The extruded blends and nanocomposites were successively thermocompressed in a hot press for 5 min at 160 °C at 200 bars in order to obtain films to carry out their characterization. The intercalated structures of the bionanocomposites have been verified by X-ray diffraction and field-emission scanning electron microscopy (FE-SEM), reported in the Supporting Information.

2.3. Characterizations

To determine the glass transition of TPS, differential scanning calorimetry (DSC) thermograms were recorded on a DSC Q2000 from TA Instruments. TPS was ground into powder using a cryogrinder and was stored at different relative humidity conditions, at RH = 97, 70, 59, 40, 25%, and dry (RH \approx 10%). Approximately 4 mg of sample was placed in sealed aluminum pans. A scan from –80 to 100 °C was run at 10 °C min^{–1}. The glass transition temperature (T_g) was determined on the first

scan at the midpoint of the calorific capacity change on the thermogram. The equilibrium water content was measured by gravimetric method. The same samples conditioned at different RH values for the DSC analysis, were dried in a ventilated oven and they were weight after 7 and 24 h in order to measure their water content.

Dynamic mechanical thermal analysis (DMTA) of the samples, conditioned at 59% of RH, was carried out using a DMA Q800 from TA Instrument in film tension mode with an amplitude of 5 μm , a frequency of 1 Hz, a force track of 125%, and a heating rate of 2 $^{\circ}\text{C min}^{-1}$. The relaxation temperatures are defined at the $\tan \delta$ profiles. Samples subjected to DMTA were cut from compression-molded thin films into regular specimens of $\approx 20 \text{ mm} \times 5 \text{ mm} \times 0.60 \text{ mm}$.

Scanning electron microscopy (SEM) images of the cryo-fracture surface of the blends and their nanocomposites, before and after etching of TPS phase in dimethyl sulfoxide (DMSO) overnight at room temperature (RT), were obtained by SEM (PHILIPS XL30 with a tungsten filament) in order to study their morphology and the compatibility of the two polymers in the blends and their nanocomposites. The polymer samples were frozen using liquid N_2 and then cryofractured. All the samples were gold/palladium coated by an automatic sputter coated Polaron SC7640. FE-SEM (Hitachi S8000) in transmission mode was used to study the melt intercalation of the polymer and to observe the filler dispersion in the nanocomposites.

Furthermore, the compatibility of the blend was investigated by confocal Raman spectroscopy using the mapping method.^[27] Raman spectra mapping is a method for generating detailed chemical images based on a sample's Raman spectrum and the Raman images were used to visualize the phase separation of the polymer blends^[28] and of their nanocomposites. For Raman mapping measurement a Renishaw InVia Reflex Raman Microscope (Wotton-Under-Edge, UK) system was used. An optical microscope was coupled to the system. The laser beam was focused on the sample with an Olympus 0.75 \times 50 microscope objective. The spatial resolution was about 1.22 μm . Calibration was done by referring to the 520 cm^{-1} line of silicon. The Raman scattering was excited using a diode laser at a wavelength of 785 nm (320 mW power). The collection time for each static spectrum (center 575 cm^{-1}) was 1 s with 100 accumulations. The spectrometer grating had 1200 lines mm^{-1} . An automatic motorized translator X-Y stage was used to collect two dimensions images. A total of about 950 spectra were measured for each sample.

Mechanical properties were determined using an Instron Universal Testing Machine at a strain rate of 150 mm min^{-1} . Tensile test measurements were performed on five dog-bone specimens with a width of 2 mm, thickness of 0.60 mm, and leaving an initial length between the clamps of 20 mm. From these experiments were obtained the Young's modulus, as the slope of the curve between 0 and 2% of deformation, the elongation at break and the maximum stress reached. Mechanical properties were studied for the specimens conditioned at RH = 59 and 97% for one week. In order to perform the DMTA and the tensile test of neat TPS a film was produced by solvent-casting. DMSO was employed as solvent and the film was cast for three days at 60 $^{\circ}\text{C}$.

Moisture absorption tests were performed after specimens were dried in a desiccator (RH = 10%) for one week. The samples were then put on the humidity chamber at RH = 97% and at 37 $^{\circ}\text{C}$ until reaching the equilibrium. The specimen were weighted every 5 min first, and the moisturizing time increased gradually when their absorption speed was slower.^[7,29] Finally, the dependency of moisture absorption on time could be obtained. The same method was used to test the dependency of moisture loss on time but the specimens were previously conditioned at RH = 97% for one week, and then they were put on a dry chamber (RH = 10%) at room temperature until reach the equilibrium.

2.3.1. Humidity-Activated Shape Memory Properties

The samples for the humidity-activated shape memory were cut from compression-molded thin films into rectangular specimens of $\approx 20 \text{ mm} \times 4 \text{ mm} \times 0.60 \text{ mm}$ and were tested using an Instron Universal Testing Machine with a temperature chamber equipped with an ultrasonic humidity generator and dry air entry. Before starting the test, samples were stored at 25 $^{\circ}\text{C}$ and at RH = 97% for at least 3 d. Samples were stretched under humidity saturated atmosphere until 80% of elongation at 10 mm min^{-1} of speed. Then, the samples were left in tension at controlled condition, first at RT at humidity saturated atmosphere for 1 h and second at RT drying for 15 h. Finally, the recovery was triggered by humidity sorption releasing the stress and under humidity saturation at 37 $^{\circ}\text{C}$. Therefore, with the aim to get a quantitative estimation of the shape memory properties of the material, the strain fixity ratio (R_f), and the strain recovery ratio (R_r) have been calculated. In particular, R_r , the ability to recover the initial shape, was taken as the ratio of the recovered strain to the fixed strain, as given by the following equation

$$R_r(N) = \frac{(\epsilon_u - \epsilon_p(N))}{\epsilon_u - \epsilon_p(N-1)} \times 100\% \quad (1)$$

R_f , the ability to fix the temporary shape, is the amplitude ratio of the fixed strain to the total strain, as presented by the Equation (2)

$$R_f(N) = \frac{\epsilon_u(N)}{\epsilon_m} \times 100\% \quad (2)$$

where ϵ_m is the deformed strain, ϵ_u is the fixed strain, ϵ_p is the recovered strain, and N is the number of cycles.

3. Results and Discussion

In order to study the effect of the nanoclay addition on the morphology of the blends, Raman mapping spectra of neat EVA, neat TPS, and B50TPS, as example, were utilized (Figure 1) in order to check their characteristic bands. The 400–700 cm^{-1} spectra region was then chosen to obtain the Raman maps. The peak at 478 cm^{-1} belongs to the skeleton vibration of pyranose ring in the glucose unit of starch as also obtained

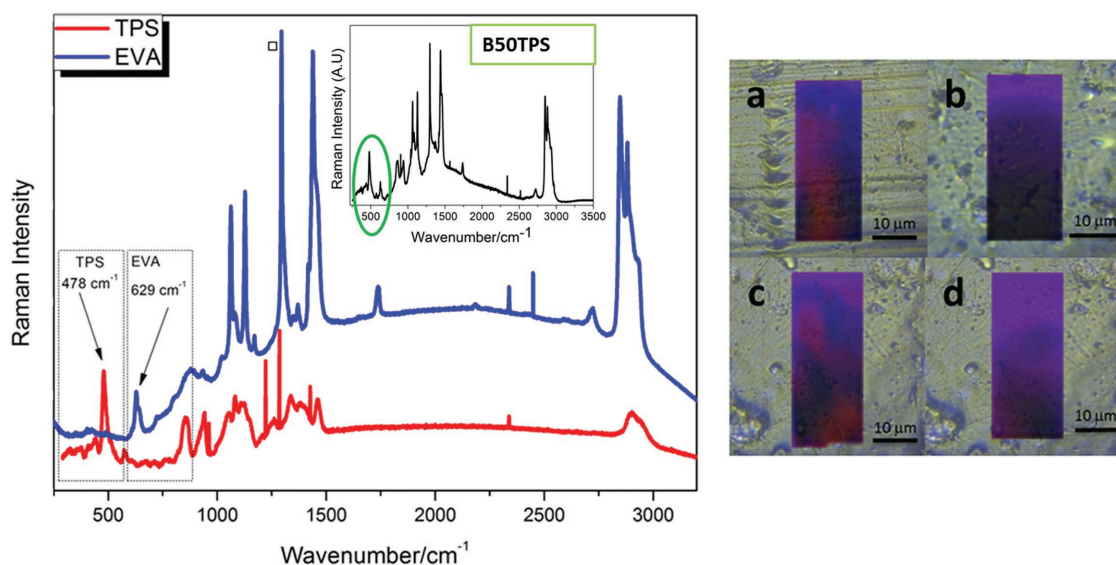


Figure 1. Raman spectra of neat EVA and neat TPS are shown on the left. In the inset, the Raman spectrum of B50TPS is reported. Video images of both blends and nanocomposites are reported on the right. a) B40TPS, b) B40TPS + 1% CLNa⁺, c) B50TPS, and d) B50TPS + 1% CLNa⁺.

by Kizil et al.,^[30] meanwhile the peak at 629 cm⁻¹ belongs to the vinyl acetate component of EVA copolymer as previously reported by Macdonald et al.^[31] The Raman spectra of B50TPS in Figure 1 showed that the peaks chosen to perform the mapping are both visible and separate.

Figure 1 displays the video images of the mapped regions of both blends and their nanocomposites. However, to better understand this analysis, a not-square-shaped region of the Raman images generated by plotting the Raman intensity variation of the scattering band at 478 and at 629 cm⁻¹, to illustrate the distribution of TPS and EVA phases, respectively, within different materials, is shown in Figure 2. In particular, three different points (named “a,” “b,” and “c”) have been taken into account just considering the different color distribution in the Raman images. The spectra from these selected points are shown in the same figure. The blue portion is related to the intensity of EVA signal from the band centered at 629 cm⁻¹ and the red portion is related to the intensity of TPS signal from the band centered at 478 cm⁻¹.

In images 1 and 3 of Figure 2 neat blends, B40TPS and B50TPS, have been reported, respectively. For the neat blends, a decrease in the peak intensity is observed at 478 cm⁻¹ (referred to TPS) as the sampled region transit from the points a to c, which almost disappears at the point b in image 1 of Figure 2. At the same time, the peak intensity at 629 cm⁻¹ (referred to EVA) increases from a to c, showing the maximum intensity in b. This is due to a phase-separated structure owing to the two-component system. It is reasonable to assume that images 1 and 3 of Figure 2 represent a spatial distribution of EVA and TPS phases. In the case of images 2 and 4 of Figure 2 where the corresponding nanocomposites have been reported, it is easy to note that the phase-separation distribution is completely different with respect to their neat blends. This fact is a consequence of the good dispersion of the nanoclays, which are able to act as compatibilizers between both phases, leading to the polymer–polymer interface as can be seen also in the FE-SEM

images in the Supporting Information. In particular, the results shown that in all selected points, a, b, and c, the intensity of the peaks does not change significantly, indicating that the phase compatibility in the nanocomposites is substantially improved with respect to the neat blends.

These results were also verified by SEM observation of the cryofracture section before and after etching the TPS component in the neat blends as well as in their nanocomposites. The SEM images for all the samples studied are shown in Figure 3. Both EVA and TPS blends were immiscible as expected. TPS is dispersed into the EVA matrix with a non-homogeneous particle size distribution. Moreover, the absence of interphase in TPS/EVA blends (Figure 3a,c), due to phase debonding, indicated a poor adhesion between both different phases. However, in the case of nanocomposites, the phase debonding is almost absent, indicating a partial miscibility between both phases, EVA and TPS probably due to the addition of nanoclays. Comparing the SEM images of the cryofracture after etching TPS phase in both neat blends and their nanocomposites, it can be noticed that in the nanocomposites a better dispersion of TPS phase and a decrease of the TPS particles dimension were observed, confirming the compatibilizer effect of nanoclays.^[32] As previously reported in the literature, nanoparticles accumulated at the polymer–polymer interface are particularly effective in changing the microstructure of immiscible polymeric blends, lowering the interfacial tension between polymers, improving the interfacial adhesion and suppressing the coalescence effect of the minor phase.^[33] Moreover, natural bentonite presents good affinity with polar polymers, which is the case of TPS and the VA content of EVA. Therefore, the presence of nanoclays in the EVA–TPS interface probably enhances EVA polarity making it more compatible with the TPS phase.

As it was previously described, the *T_g* of starchy materials is strongly influenced by their moisture content. Therefore, the effect of relative humidity on the moisture content and on the

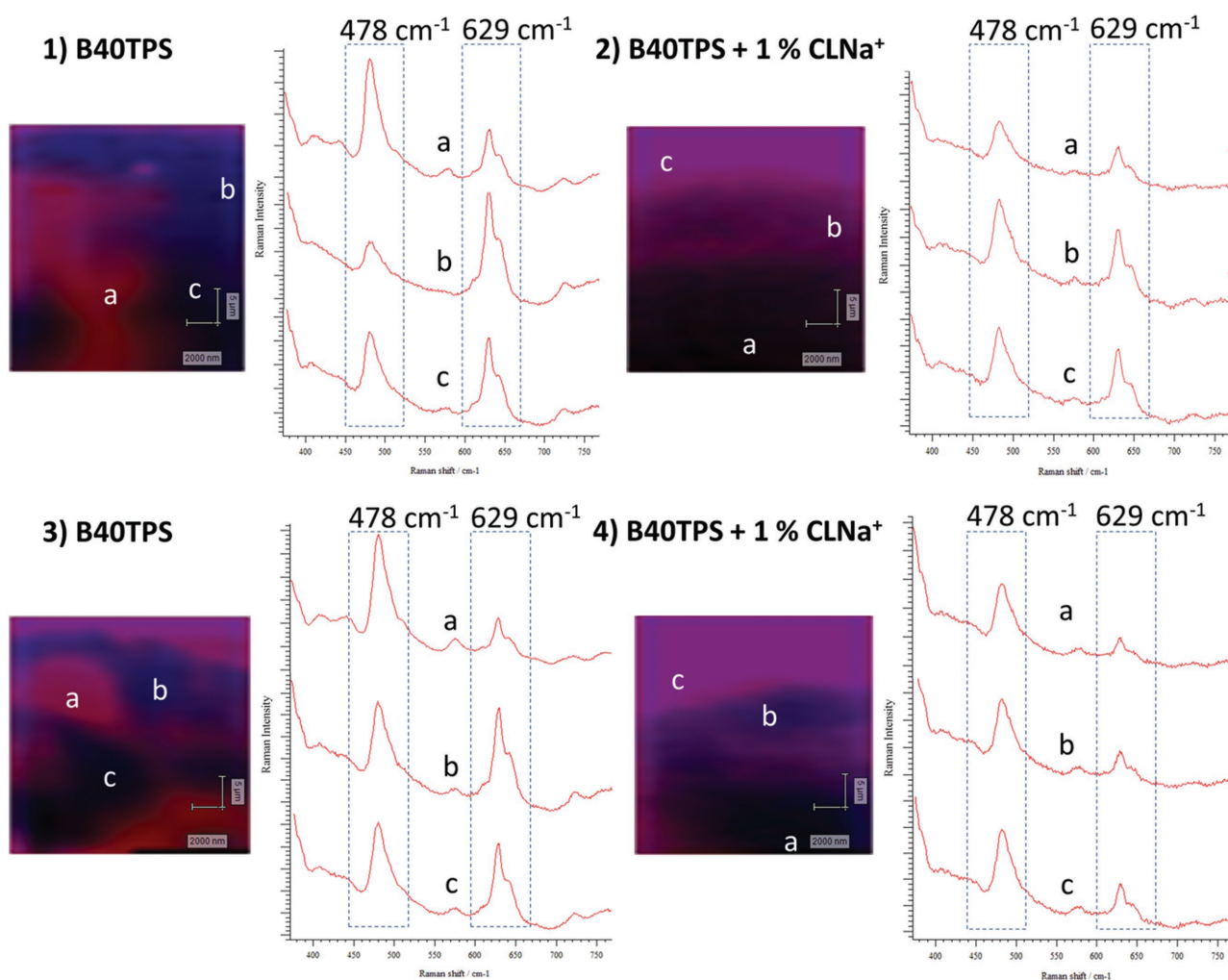


Figure 2. The Raman images and spectra generated by plotting the Raman intensity variation of the scattering band at 478 cm^{-1} and at 629 cm^{-1} for (1) B40TPS, (2) B40TPS + 1% CLNa⁺, (3) B50TPS, and (4) B50TPS + 1% CLNa⁺.

glass transition of neat TPS was studied and they are shown in **Figure 4**. The moisture content in TPS, conditioned at different RH values, was calculated by gravimetric method.

Moisture content of amorphous materials increases with the humidity level of the conditioning. In the case of neat TPS, moisture content varies from 2.8 to 9.3% when RH ranges from 25 to 70%. The evolution of T_g , determined by DSC, is related to the relative humidity. The T_g of neat TPS decreased relatively linearly from 63 to 21 °C when RH increases from 25 to 55%. The T_g values obtained in this work are in agreement with previously published data.^[34] **Figure 4** shows that a glassy/rubbery state change can be obtained at RT for RH > 55% for neat TPS. These results confirm the possibility to shift the T_g of TPS upon humidity.

The mechanical properties of these materials have been also tested at RH = 59 and 97% and the stress–strain curves obtained at room temperature and at RH = 59% are reported in **Figure 5**.

Regarding **Figure 5**, the materials (excluding TPS) show the typical curve for rubber polymer behavior, characterized by high elongation at break and low elastic modulus as it is reported in

Table 1. Furthermore, neat EVA curve shows the highest elongation at break compared with the other samples. The obtained values for the elastic modulus, elongation at break, and maximum stress for all samples are summarized in **Table 1**. **Table 1** shows a quite low elastic modulus for the EVA as expected for rubber polymers. The TPS conditioned at RH = 59% shows a typical elastic modulus of an amorphous polymer in the rubber state because at room temperature the material is above its T_g . The obtained value ($25 \pm 8\text{ MPa}$) is in agreement with values published in other works.^[35]

The results obtained by Van Soest et al.^[36] showed the dependence of the mechanical properties on the water content of the samples. They reported that at water contents lower than 5%, the materials were too brittle to be measured. The water plasticization of TPS results on a decrease of the elastic modulus from 500–1000 to 0–100 MPa and an increase of the elongation at break from 20 to 105% for a water content of 7.1 and 14.1%, respectively. At a water content of 13–15% the materials reach a maximum in the elongation at break. Above 15% of water the materials become weak and the ultimate elongation is decreased.

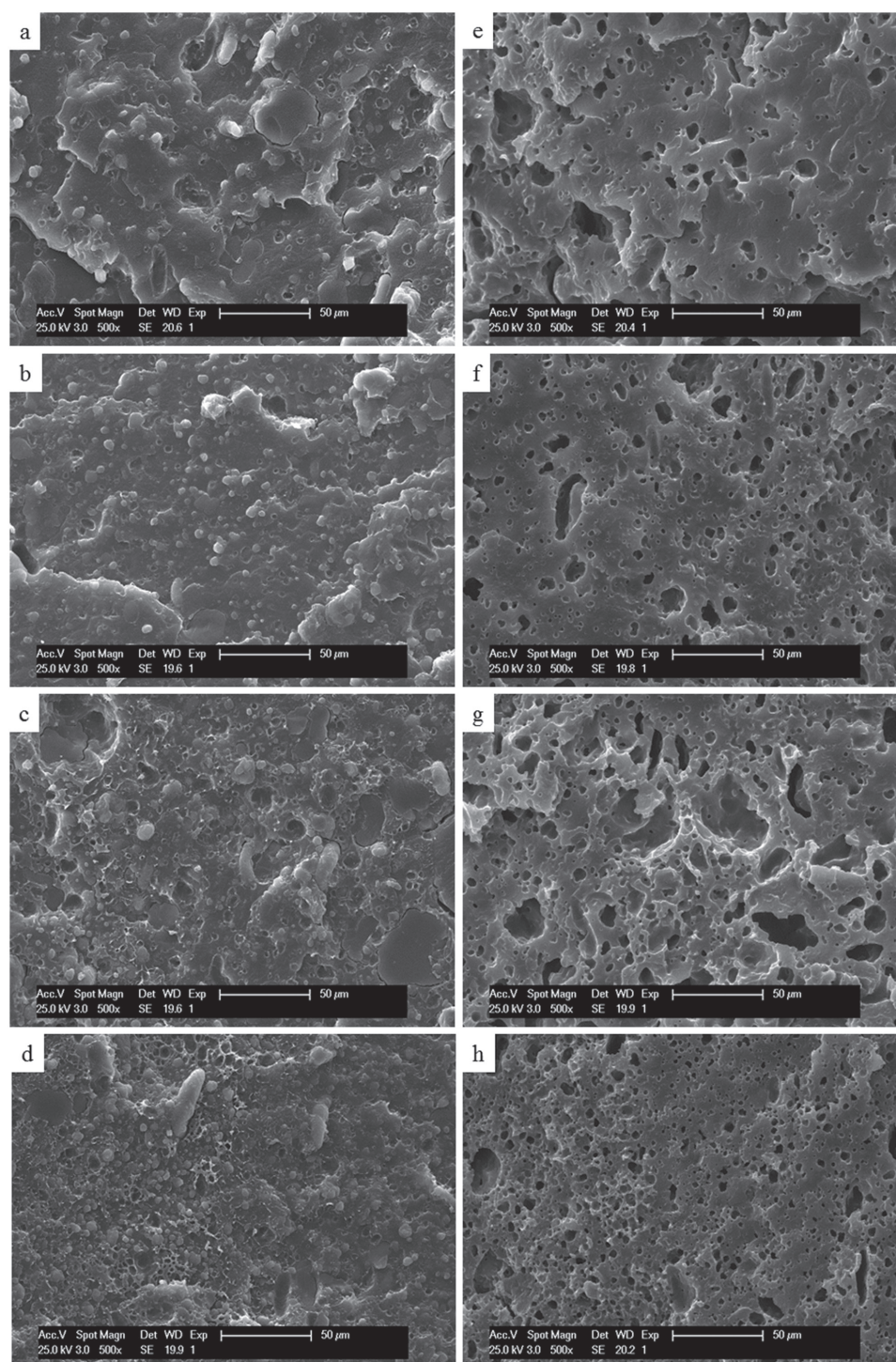


Figure 3. SEM images of EVA/TPS blends and their nanocomposites cryofractured, before etching (left) and after etching of TPS phase (right). a) B40TPS, b) B40TPS + 1% CLNa⁺, c) B50TPS, d) B50TPS + 1% CLNa⁺, e) B40TPS after etching of TPS phase, f) B40TPS + 1% CLNa⁺ after etching of TPS phase, g) B50TPS after etching of TPS phase, and h) B50TPS + 1% CLNa⁺ after etching of TPS phase.

As it was shown in Figure 4, our TPS conditioned at RH = 59% had water content at about 7% (determined for gravimetric method), and therefore this material presents a low modulus and an elongation at break of almost 60%, according to the literature. The decrease in the elastic modulus with

increasing water content is characteristic of a polymer being plasticized through its glass-to-rubber transition. At low water content, the material is glassy, and at intermediate water contents the material is rubbery.^[36] As we expect, the mechanical behavior of the blends is quite different from the mechanical

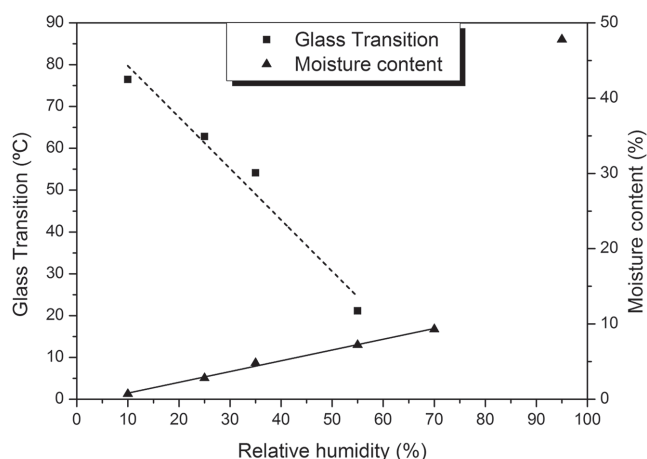


Figure 4. Effect of relative humidity on the glass transition and water content for neat TPS.

behavior of neat EVA. In fact, by increasing the amount of TPS in the blend, the elastic modulus slightly increases, whereas both the maximum stress and the elongation at break progressively decrease, so-designing more brittle materials. This phenomenon is likely due to the lower water content in the blend, compared to neat TPS, leading to a more brittle behavior for the final material. The elastic modulus of the nanocomposites slightly decreases with respect to the corresponding neat blends when 1 wt% of nanoclays was added. In both cases, a reduction of about 15% has been obtained, likely due to the compatibilizer effect of nanoclay rather than the reinforcement effect expected by the nanoclays addition. However, the good dispersion of the nanoclays was confirmed by the increase in the maximum stress of the nanocomposites compared to their corresponding neat blends. Generally, a reinforcing effect, among other factors, depends on the interfacial adhesion between the different components, which allows an efficient stress transfer between the different phases in the system.^[37] The comparisons between mechanical properties at RH = 59% and 97% in terms of elastic modulus, maximum strength and

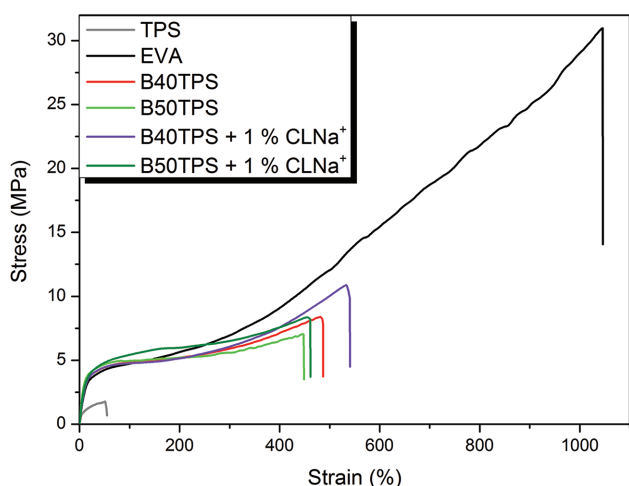


Figure 5. Stress–strain curves of all the samples studied at RH = 59%.

Table 1. Mechanical properties of all the samples.

Sample	Elastic modulus [MPa]	Maximum stress [MPa]	Elongation at break [%]
TPS	25 ± 8	1.7 ± 0.1	60 ± 10
EVA	32 ± 2	29.0 ± 5.0	1080 ± 50
B40TPS	36 ± 1	8.7 ± 0.5	500 ± 20
B40TPS + 1% CLNa+	31 ± 1	12.0 ± 1.0	600 ± 50
B50TPS	45 ± 3	6.6 ± 0.7	400 ± 60
B50TPS + 1% CLNa+	38 ± 3	7.2 ± 0.7	380 ± 50

elongation at break are shown in **Figure 6a–c**. The TPS values of mechanical properties after conditioning at RH = 97% are absent because of the impossibility to perform the test with the obtained material. The stress–strain diagram obtained for the samples conditioned at RH = 97% is reported in **Figure 6d**. As noted in **Figure 6**, the mechanical properties of the blends and nanocomposites conditioned at RH = 97% changed without any specific trend. The elastic modulus decreases when the water content increases in the materials. Similar results were reported in the bibliography for starch films conditioned at different RH values, such as RH = 32, 58, and 90%.^[38] This variation is more evident in the blends compared to the nanocomposite and it is higher for the B50TPS sample. Meanwhile, tensile strength increases with the water content, probably because of the recrystallization phenomenon of the TPS. Indeed, when starchy materials are stored above their T_g , the crystallization is promoted thanks to its chain mobility. There was previously reported in the literature that mechanical properties of plasticized samples, presented a low increase in crystallinity during storage.^[39]

Van Soest et al. studied the influence of glycerol and water content on the structure and properties of extruded starch plastic sheets during aging.^[40] They demonstrated that starch materials above their glass transition temperature were soft, almost behaving as a gel just, after extrusion. During the first week of storage, the strength and stiffness increased rapidly. The differences between the material properties before and after storage were ascribed to the formation of an entangled starch matrix by starch chain–chain associations that are related to plasticizer content. However, the sample B40TPS + 1% CLNa⁺ conditioned at RH = 97% presents a tensile strength higher than its corresponding neat blend. Regarding the elongation at break, it is easy to note that a dual behavior is shown here. For the samples containing 40 wt% of TPS the elongation at break decrease when the samples were conditioned at RH = 97%, on the other hand, samples containing 50 wt% of TPS showed an increase of the same property. For the nanocomposites, this variation is higher than for the neat blends.

In order to study the main thermomechanical relaxation of our system, DMTA analysis was performed. The evolution of the storage modulus (E'), loss modulus (E''), and damping factor ($\tan \delta$) as a function of temperature, measured over the temperature range –80 to 90 °C, for neat TPS and EVA as well as for neat blends and their nanocomposites, conditioned at 59% of RH, are presented in **Figure 7**. The storage modulus drop (**Figure 7a**) associated with the glass transition

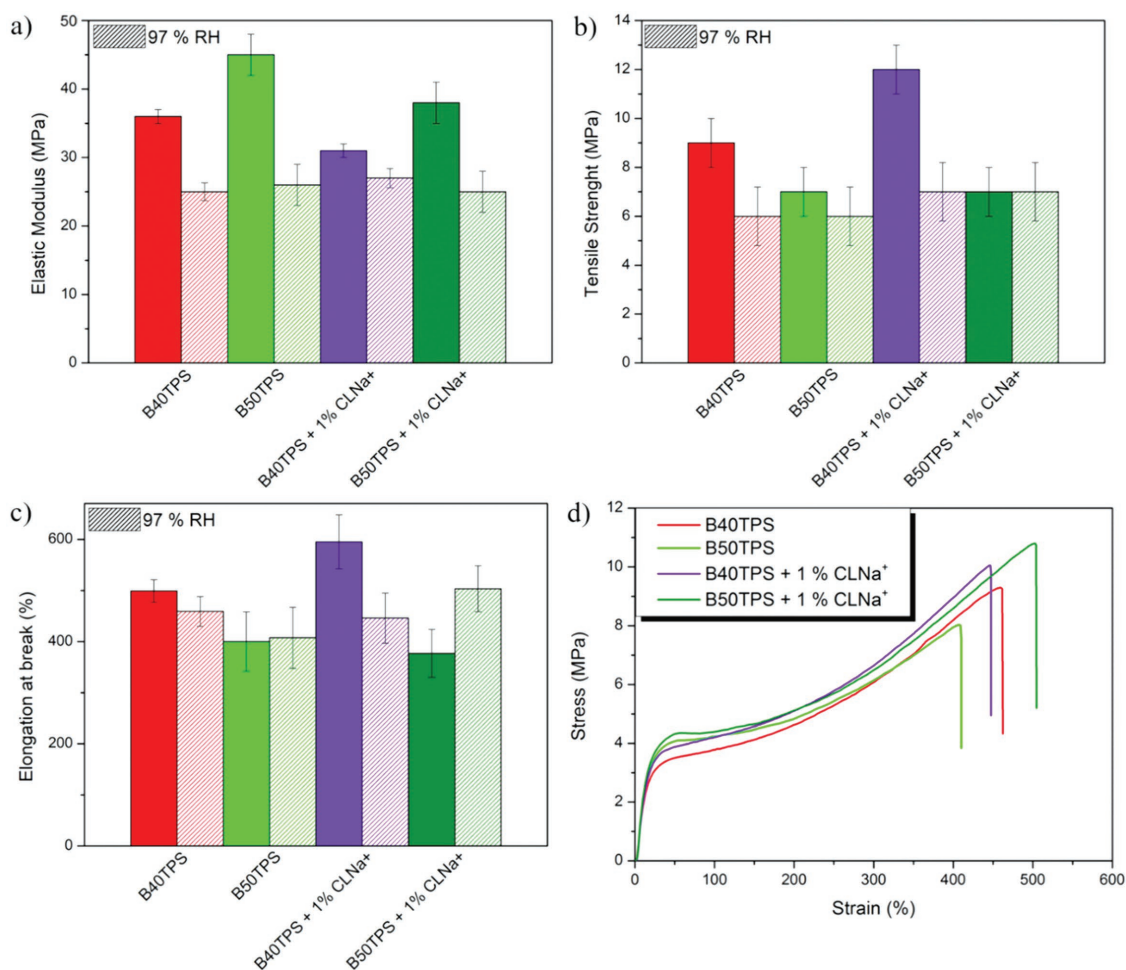


Figure 6. Comparison of mechanical properties of all blends and their nanocomposites conditioned at 59 and 97% of RH. a) Elastic modulus, b) tensile strength, and c) elongation at break. d) Stress–strain diagram of the sample conditioned at 97% of RH.

(β -relaxation) of EVA is about two orders of magnitude for all the samples. This is notably different for many other semicrystalline polymers, such as polyethylene, for which the glass transition also occurs below room temperature but the associated modulus drop is rather minimal due to the predominance of the crystalline phase.^[20] As a result, the samples containing EVA are soft at room temperature despite their semicrystalline character and they have low modulus values, according to the tensile results. Indeed, the room temperature moduli obtained from the stress–strain curves were within the range of 32 ± 2 MPa (for neat EVA), confirming the softness of all the samples. EVA modulus shows a strong dependency on the temperature. This change is accompanied by a peak in loss modulus curve at -28 °C, confirming the value obtained by DSC analyses (-26 °C) (see Figure S2, Supporting Information). Regarding the $\tan \delta$ evolution, EVA has a broad T_g , between -30 and 10 °C due to the glass transition and the PE crystals relaxation overlapping as reported in literature.^[41] Another small peak appear in the $\tan \delta$ curve at 42 °C due to the melting of smallest crystals as previously demonstrated.^[42]

In the case of neat TPS, the storage modulus falls in two steps, the first between -80 and -30 °C and the second one

between -30 and 20 °C with the respective peaks in $\tan \delta$ at -52 °C and 15 °C. At temperature of -70 °C, the TPS exhibits a high storage modulus values around 6000 MPa, confirming the rigidity of the frozen structure below T_g . It was previously reported in the literature that for starchy materials constituted by the three-constituent system as water–glycerol–starch, the roles of both competing plasticizer (glycerol and water) are dependent on their respective concentration.^[43] The results observed in Figure 7 show that using 25 wt% of glycerol leads to two relaxations of a phase-separate system on neat TPS curve. The first peak in the $\tan \delta$ curve, termed β -relaxation, is due to a starch-poor phase rich in glycerol–water content. The glass transition of this phase decreases with increasing water content but is largely independent of glycerol content. The upper peak in the $\tan \delta$ curve of neat TPS, termed α -relaxation, is due to a starch-rich phase. Forssell et al.^[34] previously reported this behavior and demonstrated that in both cases the glass transition temperature is depressed by the addition of water. At room temperature, the TPS (conditioned at RH = 59%) showed storage modulus values about 250 MPa (Figure 7a). For the blends and their nanocomposites (conditioned at RH = 59%), the DMTA results are in agreement with the tensile test results.

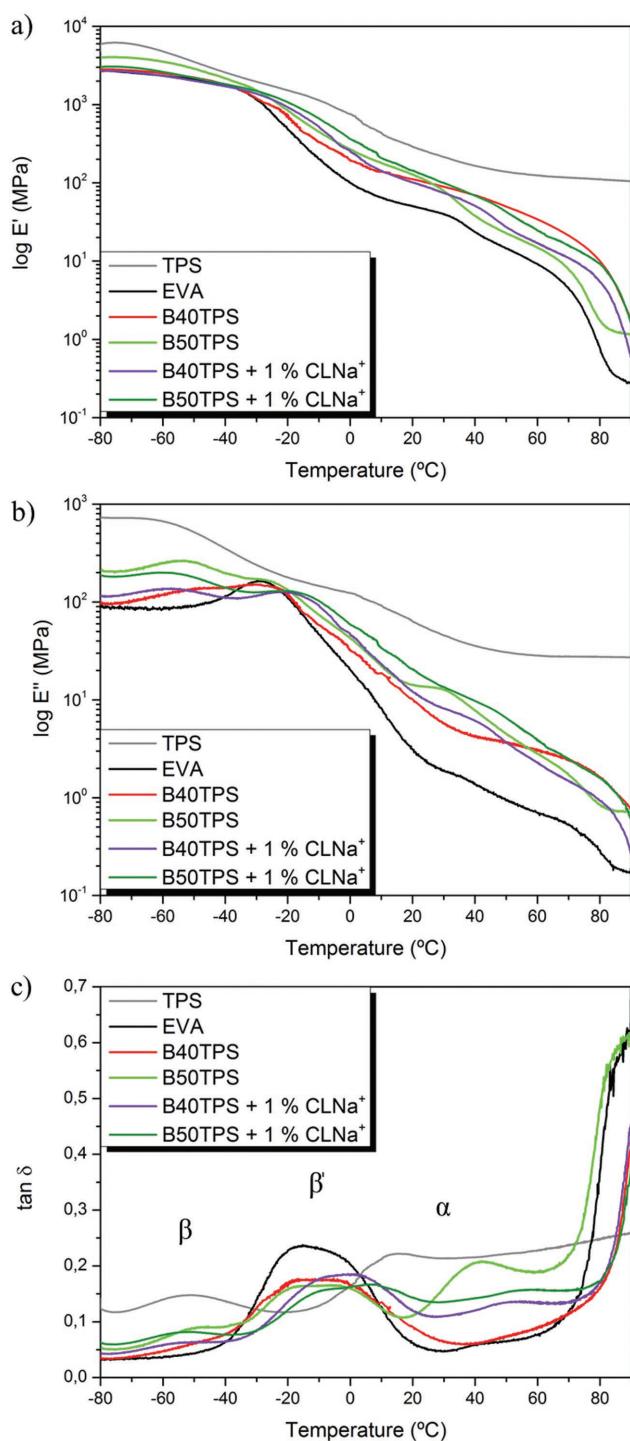


Figure 7. Dynamic mechanical thermal analysis. a) Storage modulus, b) loss modulus, and c) $\tan \delta$ for all the samples.

Indeed, increasing the TPS content in the blends the storage modulus (DMTA analysis) and the elastic modulus (in tensile test) increased, mostly in the B50TPS sample, whereas for B50TPS + 1% CLNa⁺, E' decreased. This confirms the compatibility action of nanoclays. All the blends and nanocomposites showed the typical relaxations belonging to neat EVA and

neat TPS without any shift, although the β -relaxation of TPS is shifted at higher temperatures. Only in the case of B40TPS, there was an overlapping of the EVA β -relaxation and the TPS β -relaxation, while the TPS α -relaxation almost disappeared. This behavior is likely due to the possible presence of a certain degree of miscibility between both polymers at this blend composition. It was previously reported for EVA/TPS blends that despite the fact that the system is immiscible, a certain degree of miscibility could exist and the cohesive energy of the blend can be higher than that of the separated components. Moreover, highly polar polymer mixtures able to form hydrogen bonds show very complex behavior.^[44]

In our previous work,^[1] a preliminary humidity-activated shape memory test for all the samples was performed. In this contribution, some additional investigations were performed in order to better explain the mechanism involved in the humidity-activated shape memory effect. This mechanism depends on the plasticizing effect of humidity on starchy materials. As it was previously described in this work, the T_g of the material decreases upon the water content. Moreover, in order to define how many hours are needed to activate both programming and recovery steps in the humidity-mechanical cycles used for the evaluation of the humidity-activated shape memory behavior, the dependency of moisture loss as well as of the absorption as a function of time were studied. In our previous work, we performed the recovery step of the humidity-activated cycles at 37 °C in order to shorten the recovery time of the humidity-activated cycles.^[1] In particular, our objective is to lower the T_g below RT by means of only humidity and then accelerate the recovery process thanks to the human body temperature. At this temperature, the recovery process is faster for two reasons: it is performed at least at 15 °C above the T_g of TPS to get high chain mobility and it was previously demonstrated in literature that the kinetics of absorption phenomena increases at higher temperature.^[7] For this reason, in our work, moisture absorption tests were performed directly at 37 °C. **Figure 8a,b** reports the dependencies of both moisture loss (fixing temporary shape) and moisture absorption (original shape recovery) with time for all the samples. In **Figure 8a**, it can be observed that TPS loses moisture very quickly within the first 300 min. Then, it tends to reach its saturated state after 1500 min at room temperature. In addition, it was observed that the slope of moisture loss in TPS was much higher than that in the blends and their nanocomposites, indicating higher kinetics for neat TPS. As expected, the moisture loss and absorption is higher for neat TPS. Whereas in B50TPS + 1% CLNa⁺ the moisture loss and absorption seems to be slightly faster than B50TPS, meanwhile the sample B40TPS + 1% CLNa⁺ did not show the same behavior. This sample reached its saturated state latest than the other blends and nanocomposites and the water content lost was higher than the other samples. Indeed, in **Figure 8a** is possible to note that B40TPS + 1% CLNa⁺ reached the saturated state after 4500 min rather than 1700 min like the other samples, while B40TPS + 1% CLNa⁺ lost more than 20% of water. Moreover, the slope of moisture loss for B40TPS + 1% CLNa⁺ was much higher than that of its corresponding blend, suggesting higher kinetics. The same trend is shown in **Figure 8b** for moisture absorption.

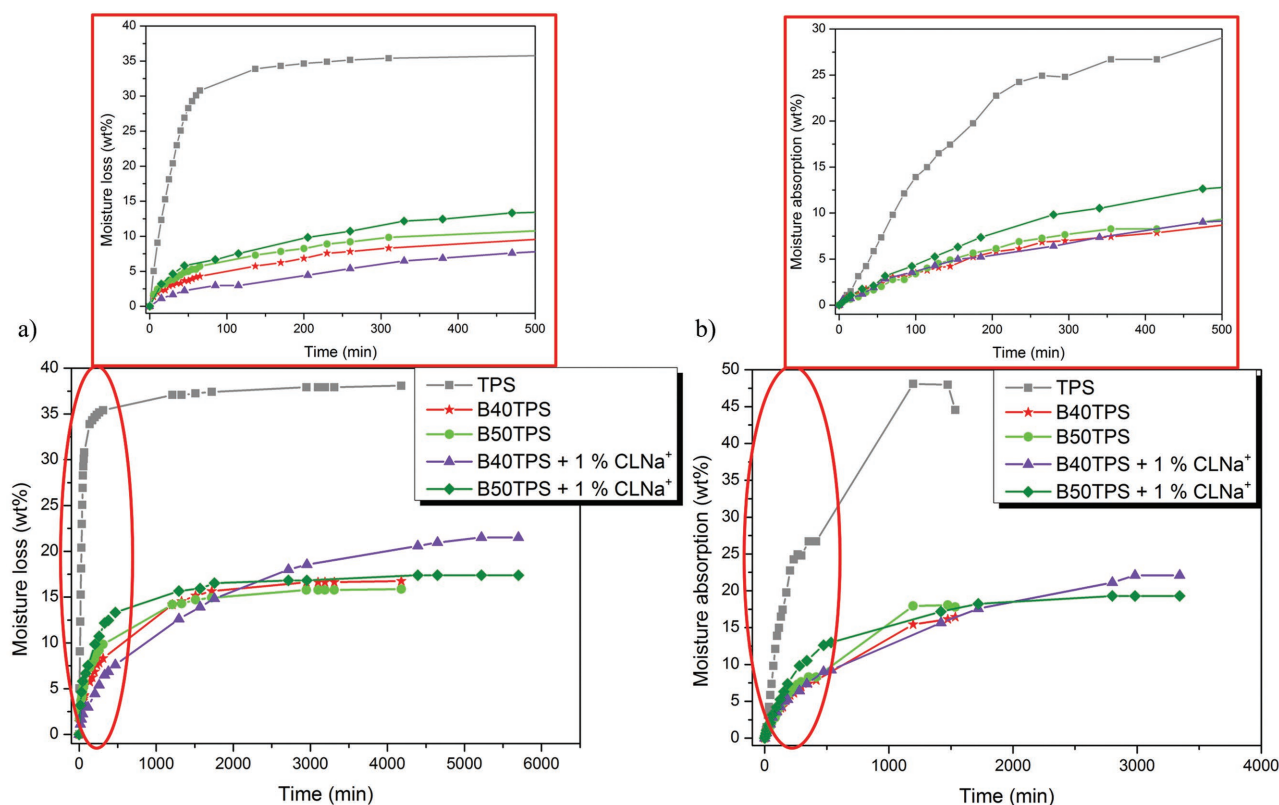


Figure 8. Dependencies on time of a) moisture loss (at RH = 10% and room temperature) and b) moisture absorption (at RH = 90% and 37 °C). In the inset, the zoomed portion is given.

The results show that the different TPS contents in the blends and their nanocomposites affects the rate of the moisture loss as well as the absorption phenomena while the presence of EVA did not inhibit the humidity-responsiveness of TPS. However, although the moisture loss and absorption phenomena mainly depends on the amount of TPS in the blend, it seems that for the nanocomposites, where the TPS domains are smaller than the corresponding blends, the rate of the moisture loss and absorption is higher than for the respective neat blends.

Finally, in order to study the humidity-activated shape memory response of the bionanocomposites and their neat blends, the following parameters were optimized for the humidity-mechanical cycles:

- Programming: conditioning the sample at room temperature and at humidity saturated atmosphere for 7 h. Stretching the samples until 80% of elongation and, after keeping the sample for 1 h at humidity saturated atmosphere, it was dried under constant stress at room temperature for 15 h.
- Recovery: releasing the stress in dry condition and recover under humidity saturated atmosphere at 37 °C for 7 h.

The 3D stress–strain–humidity cycles and the 2D stress–strain diagram were determined for all the samples studied (**Figure 9**). In order to evaluate the reproducibility of the shape memory properties, four different humidity-mechanical cycles were completed for each sample. The values obtained in every cycle for both the R_r and the R_f are summarized in **Table 2**.

The values reported in **Table 2** reflect the very good ability to recover the initial shape, showing R_r values higher than 80%. The nanocomposites did not show an evident increase in term of R_r compared to the blends through the presence of the hydrophilic nanofiller. Moreover, the ability to fix the temporary shape slightly decreased during the cycles and the nanocomposites showed higher values of R_f than the corresponding blend. When TPS content increases, in both blends and nanocomposites, better values of R_r were obtained as a result of the increase in the hydrophilic component of the materials studied.

4. Conclusions

In summary, humidity-activated shape memory effects on bionanocomposites based on blends of EVA and TPS reinforced with 1 wt% of CLNa⁺ was investigated. The plasticizing effect of water for starchy materials was used with the aim to humidity-activate the shape memory properties of the blends and their bionanocomposites. The shape memory results of both blends and their nanocomposites reflect the very good ability to humidity-activated recover of the initial shape with values higher than 80%. Moreover, the ability to fix the temporary shape of these systems is very good, especially when nanofillers are added. Moreover, the compatibilizer effect of natural bentonite was demonstrated by scanning emission microscopy and mapping by confocal Raman spectroscopy. This kind of materials could be used for biomedical applications exploiting the hydrophilic

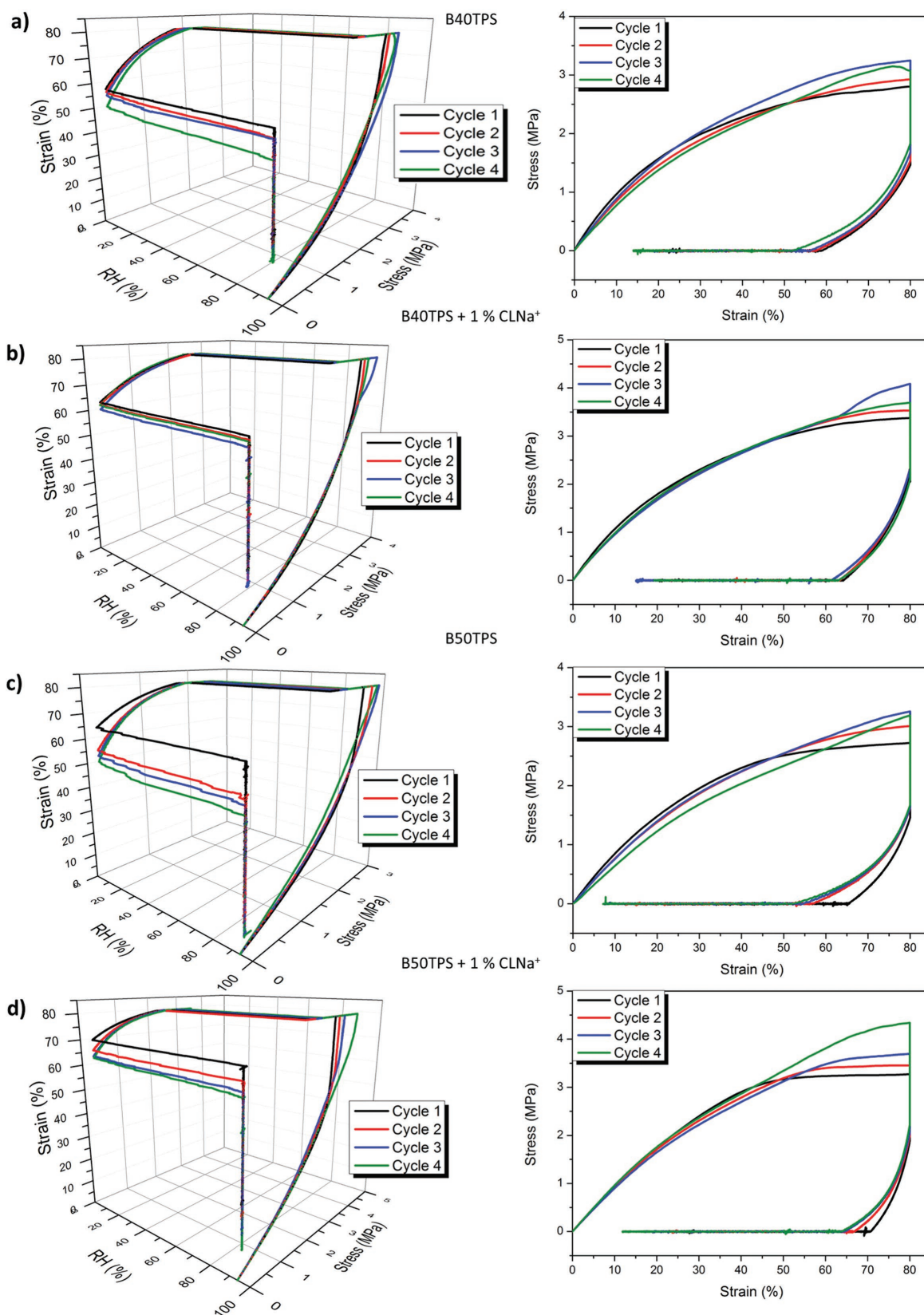


Figure 9. 3D stress–strain–humidity cycles and the 2D stress–strain diagram for a) B40TPS, b) B40TPS + 1% CLNa⁺, c) B50TPS, and d) B50TPS + 1% CLNa⁺.

Table 2. Values of R_i and R_f for the humidity-activated shape memory test for all the samples studied.

Sample	R_i [%]				R_f [%]			
	1	2	3	4	1	2	3	4
B40TPS	67	69	78	78	74	76	70	65
B40TPS + 1% CLNa ⁺	72	82	79	74	80	80	77	79
B50TPS	71	84	86	89	81	71	67	65
B50TPS + 1% CLNa ⁺	64	70	77	84	88	84	81	80

character of starch as a possibility instead of a problem. Indeed, it is possible to activate their shape memory effect by means of only humidity at the human body temperature.

Supporting Information

Supporting Information is available from the Wiley Online Library or from the author.

Acknowledgements

The authors are indebted to the Spanish Ministry of Economy, Industry and Competitiveness MINEICO (MAT2013-48059-C2-1-R) and to the Regional Government of Madrid (S2013/MIT-2862) for their economic support. L.P. acknowledges MINEICO for the “Ramon y Cajal” (RYC 2014–15595) contract. J.-M.R. and P.D. are grateful to the “Region Wallonne” and European Community (FEDER, FSE) in the excellence program OPTI²MAT for their financial support. UMONS thanks the “Belgian Federal Government Office Policy of Science (SSTC)” for general support in the frame of the PAI-7/05 and “Région Wallonne for financial support FEDER (LCFM_BIOMAT & BIORGEL). J.-M.R. is an FNRS-FRS research associate (Belgium). The authors thank CSIC for the I-LINK project, I-LINK1149.

Conflict of Interest

The authors declare no conflict of interest.

Keywords

blends, compatibilizer effect, EVA, humidity-mechanical cycles, shape memory, TPS

Received: July 27, 2017
Revised: September 27, 2017
Published online: November 15, 2017

- [1] V. Sessini, J. M. Raquez, G. Lo Re, R. Mincheva, J. M. Kenny, P. Dubois, L. Peponi, *ACS Appl. Mater. Interfaces* **2016**, *8*, 19197.
[2] L. Sun, W. M. Huang, Z. Ding, Y. Zhao, C. C. Wang, H. Purnawali, C. Tang, *Mater. Des.* **2012**, *33*, 577.
[3] L. Peponi, I. Navarro-Baena, J. M. Kenny, in *Smart Polymers and Their Applications* (Eds: M. R. Aguilar, J. S. Román), Woodhead Publishing, UK **2014**, pp. 204–236.
[4] A. Olalla, V. Sessini, E. Torres, L. Peponi, in *Multifunctional Polymeric Nanocomposites Based on Cellulosic Reinforcements* (Eds: D. Puglia, E. Fortunati, J. M. Kenny), Elsevier, USA **2016**, pp. 277–312.

- [5] A. Shirole, J. Sapkota, E. J. Foster, C. Weder, *ACS Appl. Mater. Interfaces* **2016**, *8*, 6701.
[6] A. Lendlein, R. Langer, *Science* **2002**, *296*, 1673.
[7] S. Chen, J. Hu, C.-w. Yuen, L. Chan, *Polymer* **2009**, *50*, 4424.
[8] H. Zhang, H. Wang, W. Zhong, Q. Du, *Polymer* **2009**, *50*, 1596.
[9] A. Gandini, *Macromolecules* **2008**, *41*, 9491.
[10] L. Yu, K. Dean, L. Li, *Prog. Polym. Sci.* **2006**, *31*, 576.
[11] G. Coativy, N. Gautier, B. Pontoire, A. Buléon, D. Lourdin, E. Leroy, *Carbohydr. Polym.* **2015**, *116*, 307.
[12] D. Lu, C. Xiao, S. Xu, *eXPRESS Polym. Lett.* **2009**, *3*, 366.
[13] D. LeCorre, J. Bras, A. Dufresne, *J. Nanopart. Res.* **2011**, *13*, 7193.
[14] V. Sessini, M. P. Arrieta, J. M. Kenny, L. Peponi, *Polym. Degrad. Stab.* **2016**, *132*, 157.
[15] H. M. Park, X. Li, C. Z. Jin, C. Y. Park, W. J. Cho, C. S. Ha, *Macromol. Mater. Eng.* **2002**, *287*, 553.
[16] D. Lourdin, L. Coignard, H. Bizot, P. Colonna, *Polymer* **1997**, *38*, 5401.
[17] V. Sessini, M. P. Arrieta, A. Fernández-Torres, L. Peponi, *Carbohydrate Polymers*, **2018**, *179*, 93.
[18] J. Mano, D. Koniarova, R. Reis, *J. Mater. Sci. Mater. Med.* **2003**, *14*, 127.
[19] J. Li, W. R. Rodgers, T. Xie, *Polymer* **2011**, *52*, 5320.
[20] F. Li, W. Zhu, X. Zhang, C. Zhao, M. Xu, *J. Appl. Polym. Sci.* **1999**, *71*, 1063.
[21] M. Brogly, M. Nardin, J. Schultz, *J. Appl. Polym. Sci.* **1997**, *64*, 1903.
[22] V. Tanrattanakul, T. Kaewprakob, *J. Appl. Polym. Sci.* **2011**, *119*, 38.
[23] S. Wang, Y. Zhang, Y. Zhang, C. Zhang, E. Li, *J. Appl. Polym. Sci.* **2004**, *91*, 1571.
[24] E.-R. Kenawy, G. L. Bowlin, K. Mansfield, J. Layman, D. G. Simpson, E. H. Sanders, G. E. Wnek, *J. Controlled Release* **2002**, *81*, 57.
[25] U. Nöchel, U. N. Kumar, K. Wang, K. Kratz, M. Behl, A. Lendlein, *Macromol. Chem. Phys.* **2014**, *215*, 2446.
[26] J. M. Raquez, A. Bourgeois, H. Jacobs, P. Degée, M. Alexandre, P. Dubois, *J. Appl. Polym. Sci.* **2011**, *122*, 489.
[27] S. Huan, W. Lin, H. Sato, H. Yang, J. Jiang, Y. Ozaki, H. Wu, G. Shen, R. Yu, *J. Raman Spectrosc.* **2007**, *38*, 260.
[28] I. Navarro-Baena, V. Sessini, F. Dominici, L. Torre, J. M. Kenny, L. Peponi, *Polym. Degrad. Stab.* **2016**, *132*, 97.
[29] B. D. Vogt, C. L. Soles, H.-J. Lee, E. K. Lin, W.-I. Wu, *Polymer* **2005**, *46*, 1635.
[30] R. Kizil, J. Irudayaraj, K. Seetharaman, *J. Agric. Food Chem.* **2002**, *50*, 3912.
[31] A. Macdonald, A. Vaughan, P. Wyeth, *J. Raman Spectrosc.* **2005**, *36*, 185.
[32] O. Persenaire, J. M. Raquez, L. Bonnaud, P. Dubois, *Macromol. Chem. Phys.* **2010**, *211*, 1433.
[33] M. S. de Luna, G. Filippone, *Eur. Polym. J.* **2016**, *79*, 198.
[34] P. M. Forssell, J. M. Mikkilä, G. K. Moates, R. Parker, *Carbohydr. Polym.* **1997**, *34*, 275.
[35] C. Véchambre, L. Chaunier, D. Lourdin, *Mater. Eng.* **2010**, *295*, 115.
[36] J. Van Soest, K. Benes, D. De Wit, J. Vliegthart, *Polymer* **1996**, *37*, 3543.
[37] E. George, T. Sullivan, E. Park, *Polym. Eng. Sci.* **1994**, *34*, 17.
[38] S. Mali, L. S. Sakanaka, F. Yamashita, M. V. E. Grossmann, *Carbohydr. Polym.* **2005**, *60*, 283.
[39] S. Mali, M. V. E. Grossmann, M. A. García, M. N. Martino, N. E. Zaritzky, *J. Food Eng.* **2006**, *75*, 453.
[40] J. Van Soest, N. Knooren, *J. Appl. Polym. Sci.* **1997**, *64*, 1411.
[41] L. Woo, M. T. Ling, S. P. Westphal, *Thermochim. Acta* **1994**, *243*, 147.
[42] W. Stark, M. Jaunich, *Polym. Test.* **2011**, *30*, 236.
[43] D. Lourdin, H. Bizot, P. Colonna, *J. Appl. Polym. Sci.* **1997**, *63*, 1047.
[44] A. L. Da Róz, A. M. Ferreira, F. M. Yamaji, A. J. F. Carvalho, *Carbohydr. Polym.* **2012**, *90*, 34.